

Tunable chirality of noncentrosymmetric magnetic Weyl semimetals

Rajyavardhan Ray,^{1,2,*} Banasree Sadhukhan,¹ Manuel Richter,^{1,2} Jorge I. Facio,¹ and Jeroen van den Brink^{1,2,3,†}

¹*Institute for Theoretical Solid State Physics, Leibniz IFW Dresden, Helmholtzstr. 20, 01069 Dresden, Germany*

²*Dresden Center for Computational Materials Science (DCMS), TU Dresden, 01062 Dresden, Germany*

³*Institute of Theoretical Physics, Technische Universität Dresden, 01062 Dresden, Germany*

(Dated: June 19, 2020)

Even if Weyl semimetals are characterized by quasiparticles with well-defined chirality, exploiting this experimentally is severely hampered by Weyl lattice-fermions coming in pairs with opposite chirality, typically causing the net chirality picked up by experimental probes to vanish. Here we show this issue can be circumvented in a controlled manner when both time-reversal- and inversion-symmetry are broken. To this end, we investigate chirality-disbalance in the carbide family RMC_2 (R a rare-earth and M a transition metal), showing several members to be Weyl semimetals. Using the noncentrosymmetric ferromagnet NdRhC_2 as an illustrating example, we show that an *odd* number of Weyl nodes can be stabilized at its Fermi surface by properly tilting its magnetization. The tilt direction determines the sign of the resulting net chirality, opening up a simple route to control it.

Introduction — Since their experimental discovery in the TaAs family, Weyl semimetals continue to gain interest. The non-trivial topology of this electronic phase follows from the geometrical properties [1] associated with electronic bands. Specifically, for band-crossing points, a topological invariant can be defined as the flux of Berry curvature through a surface enclosing the point. The low-energy effective theory around such a point corresponds to the Weyl equation [2], identifying the topological invariant with the corresponding Weyl fermion chirality. In lattice systems, however, Weyl nodes must come in pairs of opposite chirality [3]. Each pair having zero net chirality severely hampers experimental probes sensitive to Brillouin-zone integrated quantities from picking up the Weyl-node chirality: for this to work, one should create an overall chirality-imbalance.

The essential condition to enable the existence of Weyl nodes in the first place is broken spin degeneracy of Bloch states at a generic crystal momentum. This requires time-reversal symmetry (Θ) or inversion symmetry (\mathcal{I}) to be broken. While the first experimental confirmations of topological semimetals were achieved in Θ -symmetric compounds [4–11], magnetic compounds are naturally appealing due to the broad prospects that the interplay between the electronic structure and external magnetic fields can offer [12–21]. Still, experimentally confirmed magnetic topological semimetals are rather scarce. Two recently investigated cases are the nodal-line semimetal Co_2MnGa [22, 23] and the Weyl semimetal $\text{Co}_3\text{Sn}_2\text{S}_2$ [24–27], both centrosymmetric ferromagnets with non-trivial topology.

Here we focus on the rare-earth carbides RMC_2 , with R a rare-earth metal and M a transition metal. This broad family of compounds exhibits a diversity of Θ -breaking or \mathcal{I} -breaking phenomena [28–42] both in long-range ordered magnetic compounds [28–34] as

well as in superconducting phases [35–38] and a complex interplay between these phases and charge density waves (CDW) [39–48]. We show by consideration of available experimental information and own density-functional calculations (DFT) that RMC_2 compounds can be categorized in four classes: (I) Θ -symmetric and \mathcal{I} -broken semi-metals (YCoC_2 and LuCoC_2); (II) Θ -broken and \mathcal{I} -symmetric metals (GdRuC_2); (III) both Θ - and \mathcal{I} -broken semi-metals (PrRhC_2 , NdRhC_2 , GdCoC_2 and GdNiC_2); and (IV) insulators (LaRhC_2), the latter being of secondary interest for this work. We find that all the mentioned semi-metals possess Weyl nodes close to the Fermi energy, as summarized in Table I, where they also tend to have relatively simple and uncluttered band structures. Figure 1 illustrates the two observed structure types of the (semi-)metallic compounds.

Systems belonging to class III are of particular interest as they allow for a specific demonstration of the unique interplay between topology and magnetism offered by \mathcal{I} -broken symmetry. As a proof of principle, we show for NdRhC_2 how in ferromagnetic non-centrosymmetric phases tilting of the magnetization (\mathbf{m}) along a low symmetry direction produces a disbalance in the number of opposite chirality Weyl fermions near the Fermi surface: of *all* Weyl nodes the degeneracy is lifted. Further, the direction in which the magnetization is canted controls the sign of the chirality disbalance, allowing therefore to *switch* the dominant low-energy chirality of the electrons.

From Y to Lu — For compounds based on different R elements, we first present the main structural, electronic and magnetic properties of interest for this work. Our DFT results were obtained using the Generalized Gradient Approximation (GGA) [51], as implemented in FPLO-18 [52, 53] and considering for the treatment of the 4*f*-shell both the open-core approximation (OC) with R-specific 4*f* spin moment but spherical orbital occupation [54] and the GGA+*U* method with the full-localized limit for the double counting correction [55] and parameters $U = 7\text{eV}$ and $J = 1\text{eV}$. We study compounds which

* r.ray@ifw-dresden.de

† j.van.den.brink@ifw-dresden.de

TABLE I. Symmetry, magnetic ground state and, for the Weyl node closest to the Fermi energy, position, energy (ε), degeneracy (Deg) and band index of the lower branch in the band crossing (N is the number of valence electrons). Weyl nodes listed correspond to GGA results. For class II and III, the open-core (OC) approximation was applied with $\mathbf{m} \parallel [001]$. From top to bottom the compounds are presented in order of increasing unit cell volume.

Compound	Symmetry		Magnetic ground state			Weyl nodes			
	Class	\mathcal{I}	Θ	Expt.	Theory	Position	ε (meV)	Deg Band	
					OC	+ U	$(2\pi/a, 2\pi/b, 2\pi/c)$		
LuCoC ₂	I	-	+	NM ^a	NM	NM	(0.362, 0.163, 0)	90	4 $N-1$
YCoC ₂	I	-	+	NM ^b	NM	NM	(0.366, 0.173, 0)	61	4 $N-1$
GdCoC ₂	III	-	-	$T_C=15\text{K}^c$	FM	FM	(0.347, 0.206, 0.171)	34	4 $N-1$
GdNiC ₂	III	-	-	$T_N=20\text{K}^{d,e}$	FM	FM	$(-1/2, 0, 0.487)$	108	2 N
GdRuC ₂	II	+	-	$T_C=45(3)\text{K}^f$	FM	FM	(0.074, 0.178, 0)	15	4 $N-2$
NdRhC ₂	III	-	-	$\theta_{CW}\sim 0\text{K}^{g,h}$	FM	FM	(0.393, 0.233, -0.199)	43	4 N
PrRhC ₂	III	-	-	$\theta_{CW}\sim -13\text{K}^{g,h}$	AFM	FM	(0, 0.158, -0.221)	9	4 $N-1$

^a Ref. [40]; ^b Ref. [50]; ^c Ref. [33]; ^d Ref. [31]; ^e Ref. [39]; ^f Ref. [30]; ^g Ref. [28]; ^h Ref. [29]

have already been synthesized, including R = Y, La, Nd, Pr, Gd or Lu, and M = Co, Rh, Ni or Ru [28, 29, 31, 40], and use the lattice parameters from *The Materials Project* [56] (see the Supplementary Material (SM) [57] for further details). Table I includes available experimental data. For most of the compounds, we find that the DFT calculations agree with the reported magnetic properties. In order to analyze the electronic properties of the whole family on the same footing, we will fix in the following the quantization axis along the

in-plane direction [001].

We find that the compounds involving rare earths with empty or completely filled f -shells, R = Y, La or Lu, result in Θ -symmetric non-magnetic (NM) states, in agreement with experiment [29, 40, 50]. Among these, LaRhC₂ is the only system that crystallizes in the noncentrosymmetric tetragonal space group $P4_1$ [29] and displays an insulating electronic structure (see SM [57]). Opposed to this, YCoC₂ and LuCoC₂ grow in the noncentrosymmetric orthorhombic space group $Amm2$ [40, 50] and exhibit a semi-metallic band structure [see Fig. 2(a) and SM [57]]. Four bands dominate the energy spectrum of LuCoC₂ near the Fermi energy. These arise from hybridized Co- d , C- p and R- $5d$ states (referred to as pd states from now on). The same characteristic four bands are present at low energy for other compounds with M = Co or Rh [Fig. 2(b), (c), (e)]. On the other hand, compounds based on transition metals not isoelectronic to Co, namely, Ru or Ni, exhibit a shift of the Fermi energy of roughly $\pm 1\text{eV}$ [Fig. 2(d)]. This shift naturally changes the nature of the bands around the Fermi energy and, as we will see, their electronic properties.

Members of the family based on magnetic R ions are characterized as a lattice of localized moments on the R- $4f$ states coupled with the pd states via an onsite (Kondo) exchange. RudermanKittelKasuyaYosida exchange interactions between the $4f$ moments can lead to long-range magnetic order including the induced moments on the pd states. Consequently, these compounds are an interesting platform to explore how external magnetic fields, which couple primarily with the R- $4f$ states, can tune Weyl-node properties of the low-energy electronic structure associated with the pd states.

Among the magnetic compounds, those obtained by replacing Lu by magnetic rare earths while retaining the space group $Amm2$ [Fig. 1(a), (c)] belong to Class III, breaking both \mathcal{I} and Θ . For these compounds, different magnetic states have been reported. GdCoC₂ was first described as antiferromagnetic (AFM) with in-plane moments canted at 48° from the a -axis and $T_N = 15.6\text{K}$

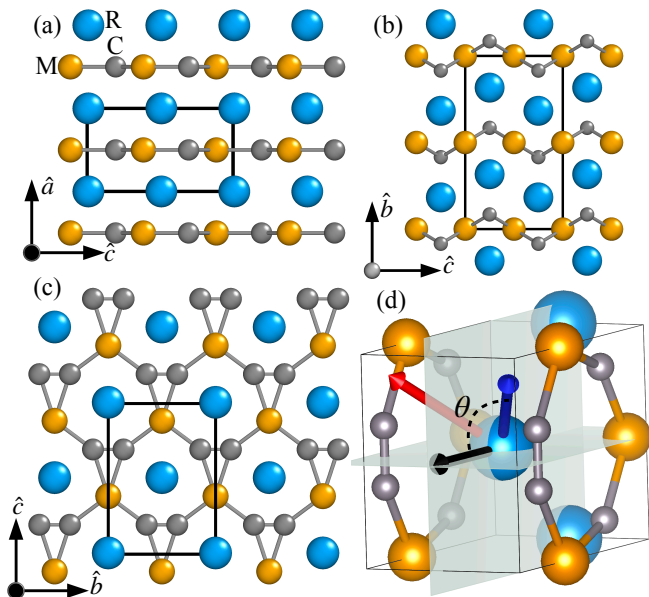


FIG. 1. Crystal structures of RMC₂. (a,c,d) Compounds with noncentrosymmetric $Amm2$ space group, and (b) $Cmcm$ space group. (a) and (b) illustrate the layered structure, formed by a quasi-planar network spanned by the MC₂ complex while the rare-earth (R) ions occupy the interstitial space between the layers. In (d), reflection symmetry planes are depicted in green while the arrows indicate directions [001] (black), [111] (red) and $[-111]$ (blue). The conventional unit cells are indicated by black solid lines.

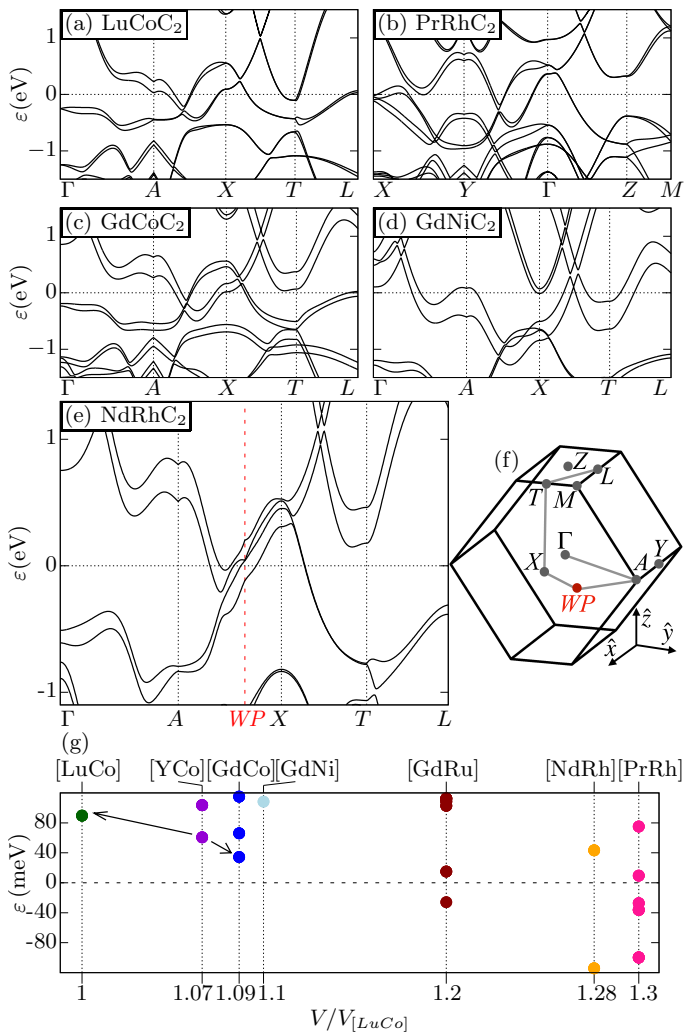


FIG. 2. (a-e) Band structures of representative rare-earth dicarbide compounds. (f) Brillouin zone. The red point corresponds to the Weyl node closest to the Fermi energy for NdRhC₂ and has coordinates $(0.665, 0.309, -0.189)\text{\AA}^{-1}$. For (b), the chosen high-symmetry points differ due to the AFM doubling of the unit-cell [49]. (g) Energy of the Weyl nodes vs. unit cell volume for all compounds considered in this work.

[31]. However, a more recent study by Meng *et al.* finds a ferromagnetic state (FM) below ~ 15 K [33]. GdNiC₂, on the other hand, as most of the Ni-based members in the family [32], presents an AFM ground-state [31]. For PrRhC₂ and NdRhC₂, experimental data is limited to high-temperature susceptibility measurements [29]. These indicate small Curie-Weiss temperatures ($\theta_{CW} \sim -13$ K and ~ 0 K, respectively) and magnetic moments in good agreement with the values expected for the trivalent R ions. GdRuC₂ exhibits an interesting contrast to the above, since it presents a transition to a FM phase but crystallizes in the \mathcal{I} -symmetric $Cmcm$ space group [Fig. 1(b)], thus belonging to Class II [30].

Our DFT results correctly capture the NM states in

YCoC₂ and LuCoC₂ and the FM states in GdCoC₂ and GdRuC₂. For NdRhC₂, we find that both GGA+OC and GGA+U predict an FM ground state. Results for PrRhC₂ are somewhat more complex, as GGA+OC and GGA+U predict as ground state AFM and FM order, respectively. The only clear deviation from experiment is found in GdNiC₂, where our calculations predict the ground state to be FM. One should, however, keep in mind that in the Ni-based carbides, a strong interplay between the magnetic state and a CDW (not explored in our calculations) has been established. In fact, there are indications that the CDW tends to compete against the FM phase [39, 43, 45, 47]. Specifically in GdNiC₂, different metamagnetic transitions have been observed under moderate external magnetic fields, yielding an interesting and complex phase diagram [39, 42, 48].

Weyl nodes — We now turn our attention to the topological properties of the electronic structure. For this, we will focus on the GGA+OC calculations. As a common reference for the following, we define for each compound the number of valence electrons as N and search for Weyl points in a relevant low-energy window $[-120, 120]$ meV, using the PYPFLO module of the FPLO package [53].

Figure 2(g) shows the energy of the identified Weyl nodes for all the compounds considered in this work, ordered as a function of their unit-cell volume (V). Table I includes the position and energy of the respective lowest energy Weyl nodes (for a complete list, see SM [57]). We also include YCoC₂ as a reference [49]. Weyl nodes at low energy are found both for Θ -symmetric and Θ -breaking cases and, among the latter, both for compounds with FM or AFM orderings.

Relations between the Weyl node structure of different compounds can also be established. For instance, an inspection of the node coordinates reveals that the four-fold degenerate Weyl nodes of lowest energy in YCoC₂, which lie in the $k_z = 0$ plane, are also present in LuCoC₂ but are higher in energy. It further suggests that on replacing Y by Gd, the large exchange field induced by the Gd-4*f* spins moves these Weyl nodes away from the $k_z = 0$ plane and to a lower energy. To confirm this, we carried out explicit computation of Weyl points in YCoC₂ under external magnetic field acting on the spin degrees of freedom. Indeed, we find that the field endows the nodes a finite k_z component.

Regarding GdNiC₂ and GdRuC₂, the Fermi energy shift associated with their different number of valence electrons with respect to GdCoC₂ is naturally in opposite directions and therefore has different consequences. On GdRuC₂, it increases the density of states and the complexity of the low-energy band structure. While it is interesting that it presents Weyl nodes close to the Fermi surface, it should not be considered as a semi-metal [49]. On the other hand, the upward shift of Fermi energy makes the Ni-based compound of strong interest. Indeed, upon this shift, a single pair of Weyl nodes – the minimum possible in a periodic system – lies ~ 100 meV

above the Fermi energy. Our calculations performed on different compounds neatly explain the origin of these Weyl nodes: The isostructural but NM LuCo_2 features twofold degenerate bands along the line X - T , forming a Dirac cone ~ 1 eV above the Fermi level [Fig. 2(a)]. The band degeneracy is lifted in the isoelectronic FM compounds [Fig. 2(c),(e)] and the Dirac cone is split into Weyl cones. Substituting Co by Ni shifts these Weyl nodes closer to the Fermi level, while keeping them along X - T [Fig. 2(d)]. While the FM phase in GdNiC_2 has only been stabilized with an external magnetic field [39, 42], it could be interesting to study this phenomenology in SmNiC_2 , where the competing CDW is suppressed [37] leading to a FM ground-state [32].

The rather large volume change caused by the substitutions $\text{Gd} \rightarrow \text{Nd}$ or Pr and $\text{Co} \rightarrow \text{Rh}$ naturally induces sizable changes in the electronic structure which remains, however, semi-metallic in NdRhC_2 and PrRhC_2 . Also, low-energy Weyl nodes are present in these compounds [Fig. 2(g)].

Pumping chirality to and through the Fermi surface — Due to the Nielsen-Ninomiya “no-go” theorem for chiral lattice fermions [3, 58], Weyl nodes come in pairs of opposite chirality [59] (which can be broken up by very strong electron-electron interactions [60, 61]). In a crystal, Weyl nodes occur in multiplets, their degeneracy being dictated by the Shubnikov group of the material which relates Weyl nodes of same or different chirality. Thus, the Weyl node degeneracy need not be even. The energy splitting between nodes of opposite chirality, a key quantity for the magnitude of different electromagnetic responses sensitive to the Weyl node chirality, actually depends on the material and external conditions. Low symmetry, in particular the absence of inversion and mirror symmetries is of the essence. Here we build on the idea of using the magnetic degrees of freedom in a \mathcal{I} -broken material to reduce the symmetry such that the Shubnikov group contains only the identity.

As a proof of principle, we consider NdRhC_2 , although the physics we discuss can be readily extended to other noncentrosymmetric magnetic compounds. In the FM ground-state, \mathbf{m} points along the $[001]$ direction and the Shubnikov group contains $\{E, m(x)\Theta, m(y)\Theta, C_2(z)\}$. Therefore, for each Weyl node away from high-symmetry lines, there are three degenerate symmetry-related partners. Any component of \mathbf{m} along a low-symmetry direction does not only break the rotation $C_2(z)$ but also the symmetries involving mirrors. Thus, starting from \mathbf{m} along $[001]$, a perturbation that cants \mathbf{m} towards, *e.g.*, $[111]$ leaves $\{E\}$ as the only symmetry element, removing all degeneracies among the Weyl nodes. The natural question is how large this effect is.

Figure 3 shows the energy of Weyl nodes in NdRhC_2 as \mathbf{m} is canted at an angle θ towards $[-111]$ (on the left) or $[111]$ (right). At $\theta = 0$, there are two sets of fourfold degenerate Weyl nodes in the energy range $[-120, 80]$ meV. Remarkably, even a moderate canting of \mathbf{m} is enough to produce experimentally meaningful en-

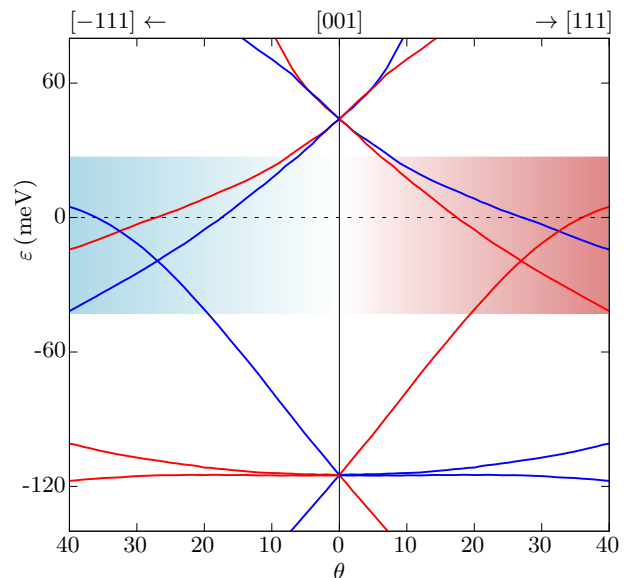


FIG. 3. Energy of Weyl nodes in NdRhC_2 as a function of the canting angle θ . Starting from the magnetization along the direction $[001]$, on the left the canting is towards $[-111]$, while on the right is towards $[111]$. Blue and red lines correspond to Weyl nodes of positive and negative chirality, respectively. The colored region highlights a wide angle range in which near the Fermi surface Weyl fermions of one chirality are majority.

ergy splittings between Weyl nodes of opposite chirality, of the order of tens of meV. Similar results for GdCoC_2 (see SM [57]) indicate that such splitting need not scale proportionally to the magnetic anisotropy field, expected to be smaller in the Gd compound than in NdRhC_2 due to the $S = J = 7/2$ state of Gd^{3+} .

The tuning of Weyl nodes to the Fermi surface at specific angles resembles the prediction for $\text{Co}_3\text{Sn}_2\text{S}_2$ [17], with the difference that in the latter case the crystal structure is centrosymmetric and each Weyl node is degenerate. This difference is crucial as \mathcal{I} always connects Weyl nodes of opposite chirality and, therefore, enforces a vanishing total chirality of the Weyl nodes at the Fermi surface. While mirror symmetries can be dynamically broken by external magnetic fields, breaking \mathcal{I} is the structural prerequisite for tuning an odd number of Weyl nodes to the Fermi surface.

The two chosen canting directions are related by a crystal mirror symmetry [Fig. 1(d)], and therefore, the chirality of the Weyl nodes reaching the Fermi surface at a certain θ is opposite for $[-111]$ and $[111]$. Thus, the canting direction provides an experimentally viable way of discarding effects not originated in the chirality disbalance. It is worth noting that this *chirality valve* is effective not only at the specific angle at which a Weyl node crosses the Fermi surface. Indeed, due to the particularly large energy trajectory of one of the nodes below the Fermi energy, in a wide range of angles for $\theta > 20^\circ$, NdRhC_2 exhibits two Weyl fermions of negative (positive) and only one of positive (negative) chirality in

a transport-relevant energy window of ± 40 meV around the Fermi energy for θ towards [111] ($[-111]$). This may generate ideal conditions to experimentally explore the role of Weyl nodes in gyrotropic and chiral magnetic effects [62, 63], in the nonlinear electric response of magnetic materials [64, 65], and in effects recently associated with the chiral anomaly like the planar Hall effect [66, 67].

Conclusions — Combination of broken inversion and broken time-reversal symmetry with a general orientation of the magnetization can lift all degeneracies among Weyl points. We have demonstrated that this allows to tune an odd number of Weyl nodes to the Fermi surface for a specific member of the RMC₂ family, which we have also shown to host various Weyl semi-metals. Our ideas can be naturally tested in all noncentrosymmetric compounds exhibiting magnetic order and provide straightforward experimental access to chiral transport.

Acknowledgments. We thank Ulrike Nitzsche for technical assistance and Klaus Koepernik for discussion. We acknowledge financial support from the German Research Foundation (Deutsche Forschungsgemeinschaft, DFG) via SFB1143 Project No. A5 and under Germany's Excellence Strategy through WzburgDresden Cluster of Excellence on Complexity and Topology in Quantum Matter *ct.qmat* (EXC 2147, Project No. 390858490). RR and MR acknowledge partial financial support from the European Union (ERDF) and the Free State of Saxony via the ESF Projects No. 100231947 and No. 100339533 (Young Investigators Group Computer Simulations for Materials Design – *CoSiMa*) during the early stages of the project. JIF acknowledges the support from the Alexander von Humboldt foundation.

-
- [1] M. V. Berry, Quantal phase factors accompanying adiabatic changes, *Proceedings of the Royal Society of London. A. Mathematical and Physical Sciences* **392**, 45 (1984).
- [2] H. Weyl, Elektron und gravitation. I, *Zeitschrift für Physik A Hadrons and Nuclei* **56**, 330 (1929).
- [3] H. B. Nielsen and M. Ninomiya, *No-go theorem for regularizing chiral fermions*, Tech. Rep. (Science Research Council, 1981).
- [4] S.-Y. Xu, I. Belopolski, N. Alidoust, M. Neupane, G. Bian, C. Zhang, R. Sankar, G. Chang, Z. Yuan, C.-C. Lee, *et al.*, Discovery of a Weyl fermion semimetal and topological Fermi arcs, *Science* **349**, 613 (2015).
- [5] L. Yang, Z. Liu, Y. Sun, H. Peng, H. Yang, T. Zhang, B. Zhou, Y. Zhang, Y. Guo, M. Rahn, *et al.*, Weyl semimetal phase in the non-centrosymmetric compound TaAs, *Nature physics* **11**, 728 (2015).
- [6] B. Q. Lv, H. M. Weng, B. B. Fu, X. P. Wang, H. Miao, J. Ma, P. Richard, X. C. Huang, L. X. Zhao, G. F. Chen, Z. Fang, X. Dai, T. Qian, and H. Ding, Experimental Discovery of Weyl Semimetal TaAs, *Phys. Rev. X* **5**, 031013 (2015).
- [7] X. Di-Fei, D. Yong-Ping, W. Zhen, L. Yu-Peng, N. Xiao-Hai, Y. Qi, D. Pavel, X. Zhu-An, W. Xian-Gang, and F. Dong-Lai, Observation of Fermi arcs in non-centrosymmetric Weyl semi-metal candidate NbP, *Chinese Physics Letters* **32**, 107101 (2015).
- [8] S. Souma, Z. Wang, H. Kotaka, T. Sato, K. Nakayama, Y. Tanaka, H. Kimizuka, T. Takahashi, K. Yamauchi, T. Oguchi, *et al.*, Direct observation of nonequivalent Fermi-arc states of opposite surfaces in the noncentrosymmetric Weyl semimetal NbP, *Physical Review B* **93**, 161112(R) (2016).
- [9] S.-Y. Xu, I. Belopolski, D. S. Sanchez, C. Zhang, G. Chang, C. Guo, G. Bian, Z. Yuan, H. Lu, T.-R. Chang, *et al.*, Experimental discovery of a topological Weyl semimetal state in TaP, *Science advances* **1**, e1501092 (2015).
- [10] N. Xu, H. Weng, B. Lv, C. E. Matt, J. Park, F. Bisti, V. N. Strocov, D. Gawryluk, E. Pomjakushina, K. Conder, *et al.*, Observation of Weyl nodes and Fermi arcs in tantalum phosphide, *Nature communications* **7**, 11006 (2016).
- [11] E. Haubold, K. Koepernik, D. Efremov, S. Khim, A. Fedorov, Y. Kushnirenko, J. van den Brink, S. Wurmehl, B. Büchner, T. K. Kim, M. Hoesch, K. Sumida, K. Taguchi, T. Yoshikawa, A. Kimura, T. Okuda, and S. V. Borisenko, Experimental realization of type-II Weyl state in noncentrosymmetric TaIrTe₄, *Phys. Rev. B* **95**, 241108(R) (2017).
- [12] A. A. Burkov, M. D. Hook, and L. Balents, Topological nodal semimetals, *Phys. Rev. B* **84**, 235126 (2011).
- [13] M. Hirschberger, S. Kushwaha, Z. Wang, Q. Gibson, S. Liang, C. A. Belvin, B. A. Bernevig, R. J. Cava, and N. P. Ong, The chiral anomaly and thermopower of Weyl fermions in the half-Heusler GdPtBi, *Nature materials* **15**, 1161 (2016).
- [14] J. Cano, B. Bradlyn, Z. Wang, M. Hirschberger, N. P. Ong, and B. A. Bernevig, Chiral anomaly factory: Creating Weyl fermions with a magnetic field, *Phys. Rev. B* **95**, 161306(R) (2017).
- [15] S. Borisenko, D. Evtushinsky, Q. Gibson, A. Yaresko, K. Koepernik, T. Kim, M. Ali, J. van den Brink, M. Hoesch, A. Fedorov, *et al.*, Time-reversal symmetry breaking type-II Weyl state in YbMnBi₂, *Nature communications* **10**, 3424 (2019).
- [16] Y. Deng, Y. Yu, M. Z. Shi, Z. Guo, Z. Xu, J. Wang, X. H. Chen, and Y. Zhang, Quantum anomalous Hall effect in intrinsic magnetic topological insulator MnBi₂Te₄, *Science* **367**, 895 (2020).
- [17] M. P. Ghimire, J. I. Facio, J.-S. You, L. Ye, J. G. Checkelsky, S. Fang, E. Kaxiras, M. Richter, and J. van den Brink, Creating Weyl nodes and controlling their energy by magnetization rotation, *Phys. Rev. Research* **1**, 032044 (2019).
- [18] D. Zhang, M. Shi, T. Zhu, D. Xing, H. Zhang, and J. Wang, Topological Axion States in the Magnetic Insulator MnBi₂Te₄ with the Quantized Magnetoelectric Effect, *Phys. Rev. Lett.* **122**, 206401 (2019).
- [19] R. C. Vidal, A. Zeugner, J. I. Facio, R. Ray, M. H. Haghighi, A. U. B. Wolter, L. T. Corredor Bohorquez, F. Cagliaris, S. Moser, T. Figgemeier, T. R. F. Peixoto,

- H. B. Vasili, M. Valvidares, S. Jung, C. Cacho, A. Alfonso, K. Mehawat, V. Kataev, C. Hess, M. Richter, B. Büchner, J. van den Brink, M. Ruck, F. Reinert, H. Bentmann, and A. Isaeva, Topological Electronic Structure and Intrinsic Magnetization in MnBi_4Te_7 : A Bi_2Te_3 Derivative with a Periodic Mn Sublattice, *Phys. Rev. X* **9**, 041065 (2019).
- [20] J. Zou, Z. He, and G. Xu, The study of magnetic topological semimetals by first principles calculations, *npj Computational Materials* **5**, 1 (2019).
- [21] Z. Liao, P. Jiang, Z. Zhong, and R.-W. Li, Materials with strong spin-textured bands, *npj Quantum Materials* **5**, 1 (2020).
- [22] G. Chang, S.-Y. Xu, X. Zhou, S.-M. Huang, B. Singh, B. Wang, I. Belopolski, J. Yin, S. Zhang, A. Bansil, H. Lin, and M. Z. Hasan, Topological hopf and chain link semimetal states and their application to Co_2MnGa , *Phys. Rev. Lett.* **119**, 156401 (2017).
- [23] I. Belopolski, K. Manna, D. S. Sanchez, G. Chang, B. Ernst, J. Yin, S. S. Zhang, T. Cochran, N. Shumiya, H. Zheng, B. Singh, G. Bian, D. Multer, M. Litskevich, X. Zhou, S.-M. Huang, B. Wang, T.-R. Chang, S.-Y. Xu, A. Bansil, C. Felser, H. Lin, and M. Z. Hasan, Discovery of topological Weyl fermion lines and drumhead surface states in a room temperature magnet, *Science* **365**, 1278 (2019).
- [24] E. Liu, Y. Sun, N. Kumar, L. Muechler, A. Sun, L. Jiao, S.-Y. Yang, D. Liu, A. Liang, Q. Xu, J. Kroder, V. S. H. Bormann, C. Shekhar, Z. Wang, C. Xi, W. Wang, W. Schnelle, S. Wirth, Y. Chen, S. T. B. Goennenwein, and C. Felser, Giant anomalous Hall effect in a ferromagnetic kagome-lattice semimetal, *Nature Physics* **1** (2018).
- [25] Q. Wang, Y. Xu, R. Lou, Z. Liu, M. Li, Y. Huang, D. Shen, H. Weng, S. Wang, and H. Lei, Large intrinsic anomalous Hall effect in half-metallic ferromagnet $\text{Co}_3\text{Sn}_2\text{S}_2$ with magnetic Weyl fermions, *Nature Communications* **9**, 3681 (2018).
- [26] N. Morali, R. Batabyal, P. K. Nag, E. Liu, Q. Xu, Y. Sun, B. Yan, C. Felser, N. Avraham, and H. Beidenkopf, Fermi-arc diversity on surface terminations of the magnetic Weyl semimetal $\text{Co}_3\text{Sn}_2\text{S}_2$, *Science* **365**, 1286 (2019).
- [27] D. Liu, A. Liang, E. Liu, Q. Xu, Y. Li, C. Chen, D. Pei, W. Shi, S. Mo, P. Dudin, *et al.*, Magnetic Weyl semimetal phase in a Kagomé crystal, *Science* **365**, 1282 (2019).
- [28] A. O. Tsokol', O. I. Bodak, E. P. Marusin, and V. E. Zavdonik, X-ray diffraction studies of ternary RRhC_2 ($\text{R}=\text{La, Ce, Pr, Nd, Sm}$) compounds), *Kristallografiya* **33**, 345 (1988).
- [29] R. D. Hoffmann, W. Jeitschko, and L. Boonk, Structural, chemical, and physical properties of rare-earth metal rhodium carbides LnRhC_2 ($\text{Ln}=\text{La, Ce, Pr, Nd, Sm}$), *Chemistry of Materials* **1**, 580 (1989).
- [30] R.-D. Hoffmann, K. H. Wachtmann, T. Ebel, and W. Jeitschko, GdRuC_2 , a ternary carbide with filled NiAs structure, *Journal of Solid State Chemistry* **118**, 158 (1995).
- [31] S. Matsuo, H. Onodera, M. Kosaka, H. Kobayashi, M. Ohashi, H. Yamauchi, and Y. Yamaguchi, Antiferromagnetism of GdCoC_2 and GdNiC_2 intermetallics studied by magnetization measurement and ^{155}Gd Mössbauer spectroscopy, *Journal of Magnetism and Magnetic Materials* **161**, 255 (1996).
- [32] H. Onodera, Y. Koshikawa, M. Kosaka, M. Ohashi, H. Yamauchi, and Y. Yamaguchi, Magnetic properties of single-crystalline RNiC_2 compounds ($\text{R}=\text{Ce, Pr, Nd}$ and Sm), *Journal of Magnetism and Magnetic Materials* **182**, 161 (1998).
- [33] L. Meng, C. Xu, Y. Yuan, Y. Qi, S. Zhou, and L. Li, Magnetic properties and giant reversible magnetocaloric effect in GdCoC_2 , *RSC Advances* **6**, 74765 (2016).
- [34] L. Meng, Y. Jia, and L. Li, Large reversible magnetocaloric effect in the RECoC_2 ($\text{RE}=\text{Ho}$ and Er) compounds, *Intermetallics* **85**, 69 (2017).
- [35] W. Lee, H. Zeng, Y. Yao, and Y. Chen, Superconductivity in the Ni based ternary carbide LaNiC_2 , *Physica C: Superconductivity* **266**, 138 (1996).
- [36] Y. Hirose, T. Kishino, J. Sakaguchi, Y. Miura, F. Honda, T. Takeuchi, E. Yamamoto, Y. Haga, H. Harima, R. Settai, and Y. nuki, Fermi surface and superconducting properties of non-centrosymmetric LaNiC_2 , *Journal of the Physical Society of Japan* **81**, 113703 (2012).
- [37] A. D. Hillier, J. Quintanilla, and R. Cywinski, Evidence for Time-Reversal Symmetry Breaking in the Noncentrosymmetric Superconductor LaNiC_2 , *Phys. Rev. Lett.* **102**, 117007 (2009).
- [38] T. Yanagisawa and I. Hase, Nonunitary triplet superconductivity in the noncentrosymmetric rare-earth compound LaNiC_2 , *Journal of the Physical Society of Japan* **81**, SB039 (2012).
- [39] K. K. Kolincio, K. Górnicka, M. J. Winiarski, J. Strychalska-Nowak, and T. Klimczuk, Field-induced suppression of charge density wave in GdNiC_2 , *Phys. Rev. B* **94**, 195149 (2016).
- [40] S. Steiner, H. Michor, O. Sologub, B. Hinterleitner, F. Höfenstock, M. Waas, E. Bauer, B. Stöger, V. Babizhetskyy, V. Levytshyy, and B. Kotur, Single-crystal study of the charge density wave metal LuNiC_2 , *Phys. Rev. B* **97**, 205115 (2018).
- [41] K. K. Kolincio, M. Roman, and T. Klimczuk, Charge density wave and large nonsaturating magnetoresistance in YNiC_2 and LuNiC_2 , *Phys. Rev. B* **99**, 205127 (2019).
- [42] N. Hanasaki, K. Mikami, S. Torigoe, Y. Nogami, S. Shimomura, M. Kosaka, and H. Onodera, Successive Transition in Rare-earth Intermetallic Compound GdNiC_2 , *Journal of Physics: Conference Series* **320**, 012072 (2011).
- [43] S. Shimomura, C. Hayashi, G. Asaka, N. Wakabayashi, M. Mizumaki, and H. Onodera, Charge-Density-Wave Destruction and Ferromagnetic Order in SmNiC_2 , *Phys. Rev. Lett.* **102**, 076404 (2009).
- [44] J. Laverock, T. D. Haynes, C. Urfeld, and S. B. Dugdale, Electronic structure of RNiC_2 ($\text{R}=\text{Sm, Gd, and Nd}$) intermetallic compounds, *Phys. Rev. B* **80**, 125111 (2009).
- [45] N. Hanasaki, Y. Nogami, M. Kakinuma, S. Shimomura, M. Kosaka, and H. Onodera, Magnetic field switching of the charge-density-wave state in the lanthanide intermetallic SmNiC_2 , *Phys. Rev. B* **85**, 092402 (2012).
- [46] G. Prathiba, I. Kim, S. Shin, J. Strychalska, T. Klimczuk, and T. Park, Tuning the ferromagnetic phase in the CDW compound SmNiC_2 via chemical alloying, *Scientific reports* **6**, 26530 (2016).
- [47] J. N. Kim, C. Lee, and J.-H. Shim, Chemical and hydrostatic pressure effect on charge density waves of SmNiC_2 , *New Journal of Physics* **15**, 123018 (2013).
- [48] N. Hanasaki, S. Shimomura, K. Mikami, Y. Nogami, H. Nakao, and H. Onodera, Interplay between charge

- density wave and antiferromagnetic order in GdNiC_2 , *Phys. Rev. B* **95**, 085103 (2017).
- [49] For this compound, we have compared our results with Ref. [50]. While we can reproduce the Weyl nodes in that work, additional search for crossings between bands $N-1$ and N discloses Weyl nodes at lower energy, as indicated in Fig. 2(g).
- [50] Y. Xu, Y. Gu, T. Zhang, C. Fang, Z. Fang, X.-L. Sheng, and H. Weng, Topological nodal lines and hybrid Weyl nodes in YCoC_2 , *APL Materials* **7**, 101109 (2019).
- [51] J. P. Perdew, K. Burke, and M. Ernzerhof, Generalized gradient approximation made simple, *Phys. Rev. Lett.* **77**, 3865 (1996).
- [52] K. Koepnik and H. Eschrig, Full-potential nonorthogonal local-orbital minimum-basis band-structure scheme, *Phys. Rev. B* **59**, 1743 (1999).
- [53] <https://www.fplo.de>.
- [54] M. Richter, Density Functional Theory Applied to 4f and 5f Elements and Metallic Compounds (Elsevier, Amsterdam, 2001) Chap. 2, pp. 87–228.
- [55] M. T. Czyzyk and G. A. Sawatzky, Local-density functional and on-site correlations: The electronic structure of La_2CuO_4 and LaCuO_3 , *Phys. Rev. B* **49**, 14211 (1994).
- [56] A. Jain, S. P. Ong, G. Hautier, W. Chen, W. D. Richards, S. Dacek, S. Cholia, D. Gunter, D. Skinner, G. Ceder, *et al.*, Commentary: The materials project: A materials genome approach to accelerating materials innovation, *APL Materials* **1**, 011002 (2013).
- [57] Supplemental material contains further information on (i) crystal structures used, (ii) methods used, (iii) effects of canting the magnetization in GdCoC_2 , (iv) band structures and density of states, and (v) Weyl nodes found.
- [58] D. Friedan, A proof of the Nielsen-Ninomiya theorem, *Communications in Mathematical Physics* **85**, 481 (1982).
- [59] E. Witten, Three lectures on topological phases of matter, *Rivista del Nuovo Cimento della Societa Italiana di Fisica* **39**, 313 (2016).
- [60] T. Meng and J. C. Budich, Unpaired Weyl Nodes from Long-Ranged Interactions: Fate of Quantum Anomalies, *Phys. Rev. Lett.* **122**, 046402 (2019).
- [61] L. Crippa, A. Amaricci, N. Wagner, G. Sangiovanni, J. C. Budich, and M. Capone, Nonlocal annihilation of Weyl fermions in correlated systems, *Phys. Rev. Research* **2**, 012023 (2020).
- [62] S. Zhong, J. E. Moore, and I. Souza, Gyrotropic Magnetic Effect and the Magnetic Moment on the Fermi Surface, *Phys. Rev. Lett.* **116**, 077201 (2016).
- [63] J. Ma and D. A. Pesin, Chiral magnetic effect and natural optical activity in metals with or without Weyl points, *Phys. Rev. B* **92**, 235205 (2015).
- [64] F. de Juan, A. G. Grushin, T. Morimoto, and J. E. Moore, Quantized circular photogalvanic effect in Weyl semimetals, *Nature communications* **8**, 15995 (2017).
- [65] T. Holder, D. Kaplan, and B. Yan, Consequences of Time-reversal-symmetry Breaking in the Light-Matter Interaction: Berry Curvature, Quantum Metric and Diabatic Motion, *arXiv preprint arXiv:1911.05667* (2019).
- [66] S. Nandy, G. Sharma, A. Taraphder, and S. Tewari, Chiral Anomaly as the Origin of the Planar Hall Effect in Weyl Semimetals, *Phys. Rev. Lett.* **119**, 176804 (2017).
- [67] T. Nag and S. Nandy, Transport phenomena of multi-Weyl semimetals in co-planar setups, *arXiv preprint arXiv:1812.08322* (2018).
- [68] K. Persson, *Materials data on YCoC₂ (SG:38) by materials project* (2016).
- [69] K. Persson, *Materials data on LuCoC₂ (SG:38) by materials project* (2016).
- [70] K. Persson, *Materials data on GdCoC₂ (SG:38) by materials project* (2017).
- [71] K. Persson, *Materials data on GdNiC₂ (SG:38) by materials project*.
- [72] K. Persson, *Materials data on NdRhC₂ (SG:38) by materials project* (2016).
- [73] K. Persson, *Materials data on PrRhC₂ (SG:38) by materials project* (2016).
- [74] K. Persson, *Materials data on GdRuC₂ (SG:63) by materials project* (2016).
- [75] K. Persson, *Materials data on LaRhC₂ (SG:76) by materials project* (2016).
- [76] B. Dorado, M. Freyss, B. Amadon, M. Bertolus, G. Jomard, and P. Garcia, Advances in first-principles modelling of point defects in UO_2 : f electron correlations and the issue of local energy minima, *Journal of Physics: Condensed Matter* **25**, 333201 (2013).
- [77] J. P. Allen and G. W. Watson, Occupation matrix control of d- and f-electron localisations using DFT $+U$, *Phys. Chem. Chem. Phys.* **16**, 21016 (2014).

SUPPLEMENTAL INFORMATION

Section S1 contains details about the crystal structures used in the calculations. Section S2 explains the methodological aspects of the calculations. Section S3 presents the results of canting the magnetization in GdCoC₂. Section S4 exhibits, in Figs. S3 – S9, the bandstructures of the considered materials on a larger Brillouin zone path and larger energy window than in the main text. Tables SII – SVII contain further information about the Weyl nodes found in the considered semimetals.

S1. CRYSTAL STRUCTURES

The structural parameters for all the compounds considered in this study were obtained from *The Materials Project* [56]. Table SI lists the space groups, lattice constants (a , b , c), primitive unit cell volumes (Vol), corresponding formula units (f.u.) per unit cell (Z), and selected bond lengths (d) for these compounds.

TABLE SI. Structural parameters for the considered compounds with the general formula RMC₂. Note that only the distance between intra-layer R-ions is listed, since the layers are separated by the lattice vector a . For systems belonging to classes I-III, the layers are defined according to Fig. 1 of the main text.

Parameter	YCoC ₂ [68]	LuCoC ₂ [69]	GdCoC ₂ [70]	GdNiC ₂ [71]	NdRhC ₂ [72]	PrRhC ₂ [73]	GdRuC ₂ [74]	LaRhC ₂ [75]
Class	I	I	III	III	III	III	II	IV
Space Gr.	<i>Amm2</i>	<i>Amm2</i>	<i>Amm2</i>	<i>Amm2</i>	<i>Amm2</i>	<i>Amm2</i>	<i>Cmcm</i>	<i>P4₁</i>
a (Å)	3.5880	3.4336	3.6336	3.6597	3.7184	3.7760	4.4766	3.9913
b (Å)	4.5141	3.4759	4.5185	4.5335	4.7308	4.7367	9.3054	3.9913
c (Å)	5.9955	5.9272	6.0277	6.03826	6.6371	6.6528	5.2503	15.4194
Z	1	1	1	1	1	1	2	4
Vol (Å ³)	48.56	45.55	49.48	50.10	58.38	59.50	109.36	245.64
$d_{R-R}^{\text{intra-layer}}$ (Å)	3.7524	3.7137	3.7666	3.7754	4.0753	4.0834	3.6681	4.0335
	4.5141	4.4759	4.5185	4.5335	4.7308	4.7367	4.4766	4.7669
d_{C-C} (Å)	1.3794	1.3796	1.3776	1.3733	1.3498	1.3496	1.4078	1.3552
d_{M-C} (Å)	1.9345	1.9092	1.9462	1.9476	2.1075	2.1135	2.16734	2.0746
	1.9873	1.9710	1.9875	2.0020	2.1679	2.1696	–	2.0867
								2.1292
								2.1662

S2. METHODS

Density functional theory (DFT) calculations were carried out using the Perdew-Burke-Ernzerhof (PBE) implementation [51] of the generalized gradient approximation (GGA) using the full-potential local-orbital (FPLO) code [52], version 18.00-57 [53]. A k -mesh with $12 \times 12 \times 12$ subdivisions was used for numerical integration in the Brillouin zone (BZ) along with a linear tetrahedron method. Spin-orbit effects were included in the self-consistent calculations via the 4-spinor formalism implemented in the FPLO code. To study the relative stability of different collinear long-range ordered states (applicable to materials belonging to classes II & III), different lower-symmetry antiferromagnetic (AFM) configurations were generated:

- **AF1**, with AFM interlayer and ferromagnetic (FM) intralayer couplings,
- **AF2**, with FM interlayer and AFM intralayer interaction,
- **AF3**, with AFM interlayer as well as AFM intralayer interaction.

Fig. S1 shows these AFM configurations for compounds belonging to classes II and III.

The description of the $4f$ elements within the framework of DFT is still a subtle problem [54]. In this work, we considered both of the widely-used approaches to treat the $4f$ -shell: the open-core (OC) approximation, and the GGA+ U scheme. In the first approach, we set the spin for R³⁺ ions according to the Hund's first rule while maintaining a spherically averaged distribution of electrons in the $4f$ shell [54]. In the second approach, to circumvent the usual

problem of multiple metastable solutions, we used the occupation matrix control [76, 77], whereby several different initial $4f$ density matrices, corresponding to +3 valence of R ions, were considered to explore the energy landscape. We used the full-localized limit of the double counting scheme with $F^0 = 7.0$ eV, $F^2 = 11.92$ eV, $F^4 = 7.96$ eV, and $F^6 = 5.89$ eV, leading to $U = 7$ eV and $J = 1$ eV. For most of the compounds, both GGA+OC and GGA+ U favors the magnetic moments to be in-plane. Therefore, we consider $\mathbf{m} \parallel [001]$ for all the compounds for brevity and comparison. While we can anticipate that the existence of Weyl nodes at low energies is a finding robust to these explored choices, we will discuss to what extent details such as position in energy and momentum can be affected in a forthcoming publication.

To study the topological properties, we constructed a tight-binding model based on maximally projected Wannier functions. In the basis set, states lying in the energy window -9.5 eV to 10 eV were considered. The Wannier basis set typically included the $5d$ and $6s$ states for R (respectively, $3d$ and $4s$ for Y), valence d and s states for M, and $2s$ and $2p$ states for C. The accuracy of the resulting tight-binding models was typically $\lesssim 15$ meV compared to the self-consistent bandstructures.

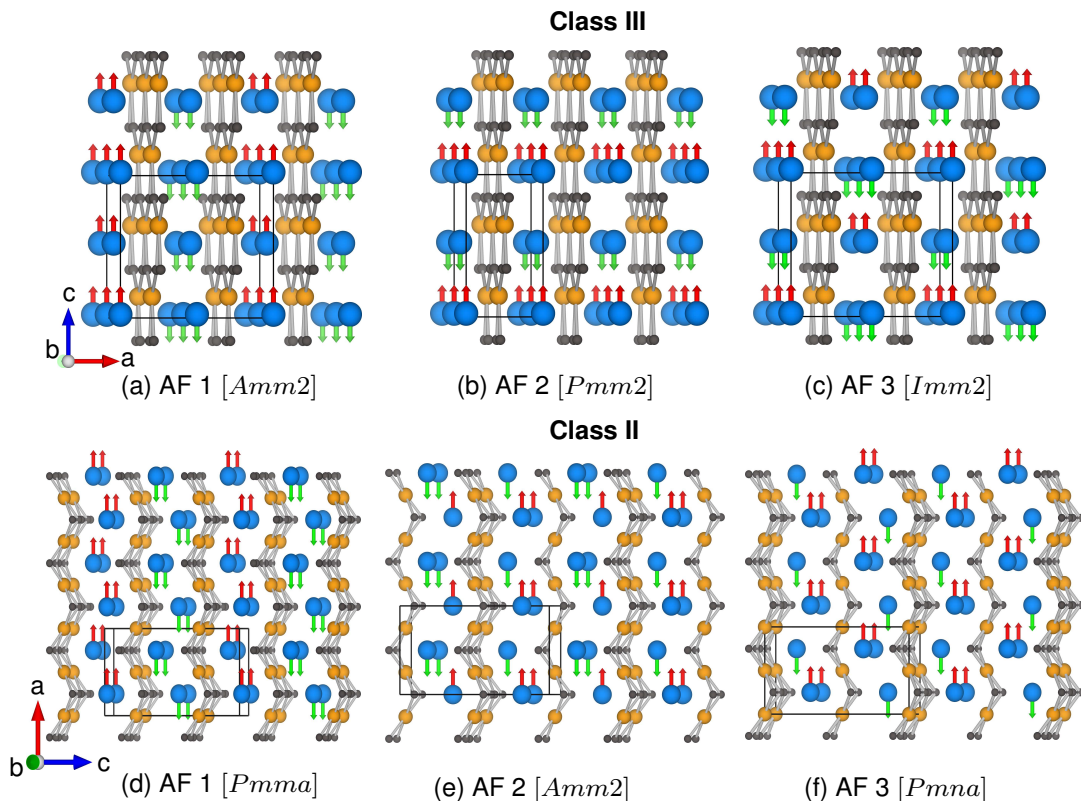


FIG. S1. AFM configurations considered for compounds belonging to the symmetry classes II and III. The R atoms, transition metal atoms and carbon atoms are, respectively, shown with blue, yellow and grey spheres. The relative spin directions on the R atoms are represented by arrows. The choice of quantization axis is only schematic. For each case, the resulting lower symmetry space groups are also indicated.

S3. WEYL NODES IN GdCoC₂

Fig. S2 shows the splitting in energy of the Weyl node closest to the Fermi energy in GdCoC₂ as the magnetization is canted from [001] to [111]. Notice that energy splittings of tens of meV are obtained, similar to the results for NdRhC₂ in the main text, regardless of the smaller magnetic anisotropy energy expected in GdCoC₂ due to the half-filled 4f shell.

It is important to realize, as these results indicate, that the energy scale associated with the splitting in energy of the Weyl nodes need not scale with the magnetic anisotropy energy. Thus, sizeable splittings can occur in materials which require significantly different external magnetic field to cant the magnetization.

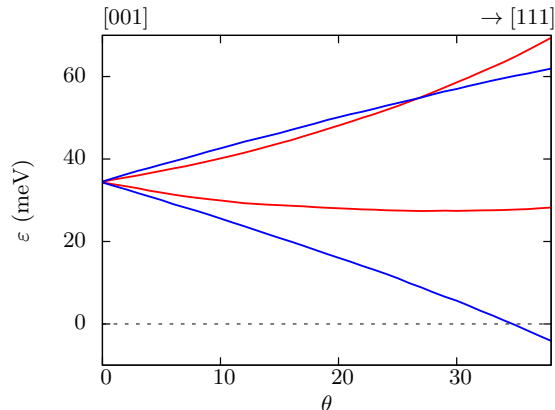


FIG. S2. Energy of the Weyl nodes as a function of the canting angle θ for GdCoC₂. Blue and red lines, respectively, correspond to Weyl nodes of positive and negative chirality.

S4. ELECTRONIC PROPERTIES

For completeness, below we provide the bandstructures and element-resolved density of states (DOS) for the different compounds considered in this work and list all the respective Weyl nodes found in the energy window between ± 120 meV.

TABLE SII. Weyl points (WPs) in YCoC₂ arising from crossing of bands ‘Band’ and ‘Band+1’. N refers to the no. of electrons in the system and, therefore, also to the valence band lying closest to the Fermi energy. Other equivalent WPs can be generated by considering the crystal symmetries $\{E, m(x), m(y), C_2(z)\}$ and the time-reversal symmetry.

Band	Energy (meV)	Position $(k_x/a, k_y/b, k_z/c)/2\pi$	χ	Deg
$N - 1$	60.7	(0.366, 0.173, 0)	1	4
	103.7	(-0.382, 0.159, 0.158)	1	8

TABLE SIII. WPs in LuCoC₂. Other details and conventions are same as in Table SII.

Band	Energy (meV)	Position $(k_x/a, k_y/b, k_z/c)/2\pi$	χ	Deg
$N - 1$	89.5	(-0.362, -0.163, 0)	-1	4

TABLE SIV. WPs in the FM-[001] phase of GdCoC₂, arising out of the crossing of the bands ‘Band’ and ‘Band +1’. The OC solution was considered. N refers to the number of valence electrons in the system and, therefore, also to the valence band closest to the Fermi energy. Other equivalent WPs can be generated by considering the symmetries: $\{E, C_2(z), m(x)\Theta, m(y)\Theta\}$.

Band	Energy (meV)	Position $(k_x/a, k_y/b, k_z/c)/2\pi$	χ	Deg
$N - 1$	34.5	(0.347, 0.206, 0.171)	1	4
N	66.1	(0.483, -0.114, -0.282)	1	4
	115.0	(0.373, 0.129, 0.187)	1	4

TABLE SV. WPs in GdNiC₂. Other details and conventions are same as in Table SIV.

Band	Energy (meV)	Position $(k_x/a, k_y/b, k_z/c)/2\pi$	χ	Deg
$N + 1$	108.3	(-0.5, 0, 0.487)	-1	2

TABLE SVI. WPs in NdRhC₂. Other details and conventions are same as in Table SIV.

Band	Energy (meV)	Position $(k_x/a, k_y/b, k_z/c)/2\pi$	χ	Deg
N	-114.1	(-0.414, -0.328, 0.220)	1	4
	43.4	(-0.393, -0.233, -0.199)	1	4

TABLE SVII. WPs in the AF1-[001] state of PrRhC₂. Other details and conventions are same as in Table SIV. The near-degeneracy of WPs between bands $(N, N + 1)$ and $(N + 1, N + 2)$ reflect that $\Theta\mathcal{T}$, where \mathcal{T} is the translation operator for shift by half a unit cell along a , is only marginally broken around these WPs.

Band	Energy (meV)	Position $(k_x/a, k_y/b, k_z/c)/2\pi$	χ	Deg
$N - 1$	9.5	(0, -0.158, -0.222)	1	4
	75.1	(-0.231, -0.203, 0)	1	4
N	-100.03	(0.1952, 0.3276, 0.2216)	1	4
	-99.55	(-0.1954, -0.3274, -0.2214)	1	4
$N + 1$	-36.19	(0.1215, 0.3542, 0.1725)	-1	4
	-36.18	(-0.1230, -0.3540, -0.1726)	-1	4
	-27.3	(-0.004, -0.363, 0.163)	1	4

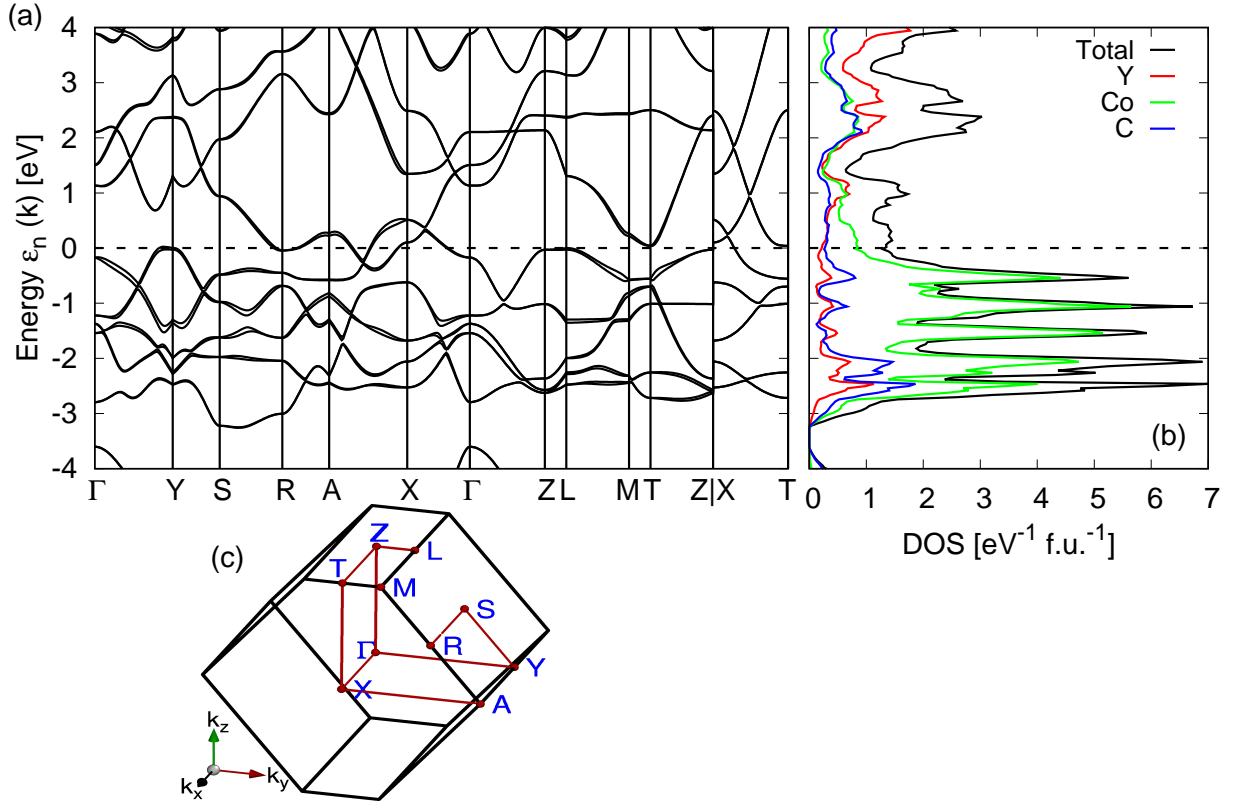


FIG. S3. Electronic properties of YCoC₂: (a) bandstructure, and (b) total and element-resolved density of states (DOS) with spin orbit effects included. The high-symmetry points are shown in (c).

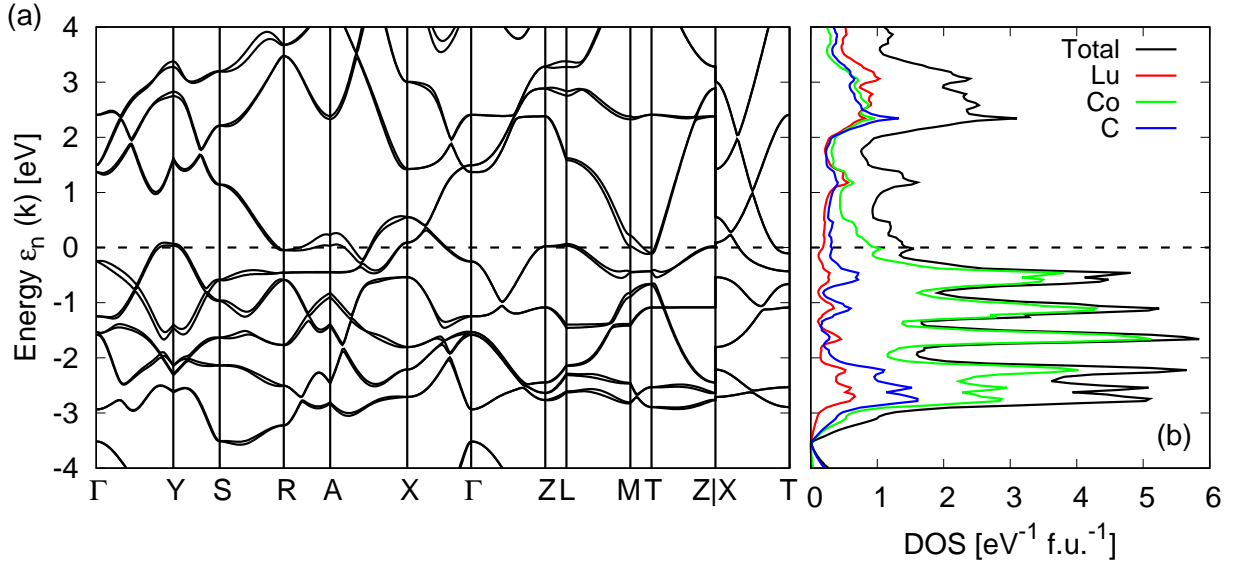


FIG. S4. Electronic properties of LuCoC₂: (a) bandstructure, and (b) total and element-resolved contributions to DOS with spin-orbit effects included. The BZ and the high symmetry points are similar to that of YCoC₂, shown in Fig. S3(c).

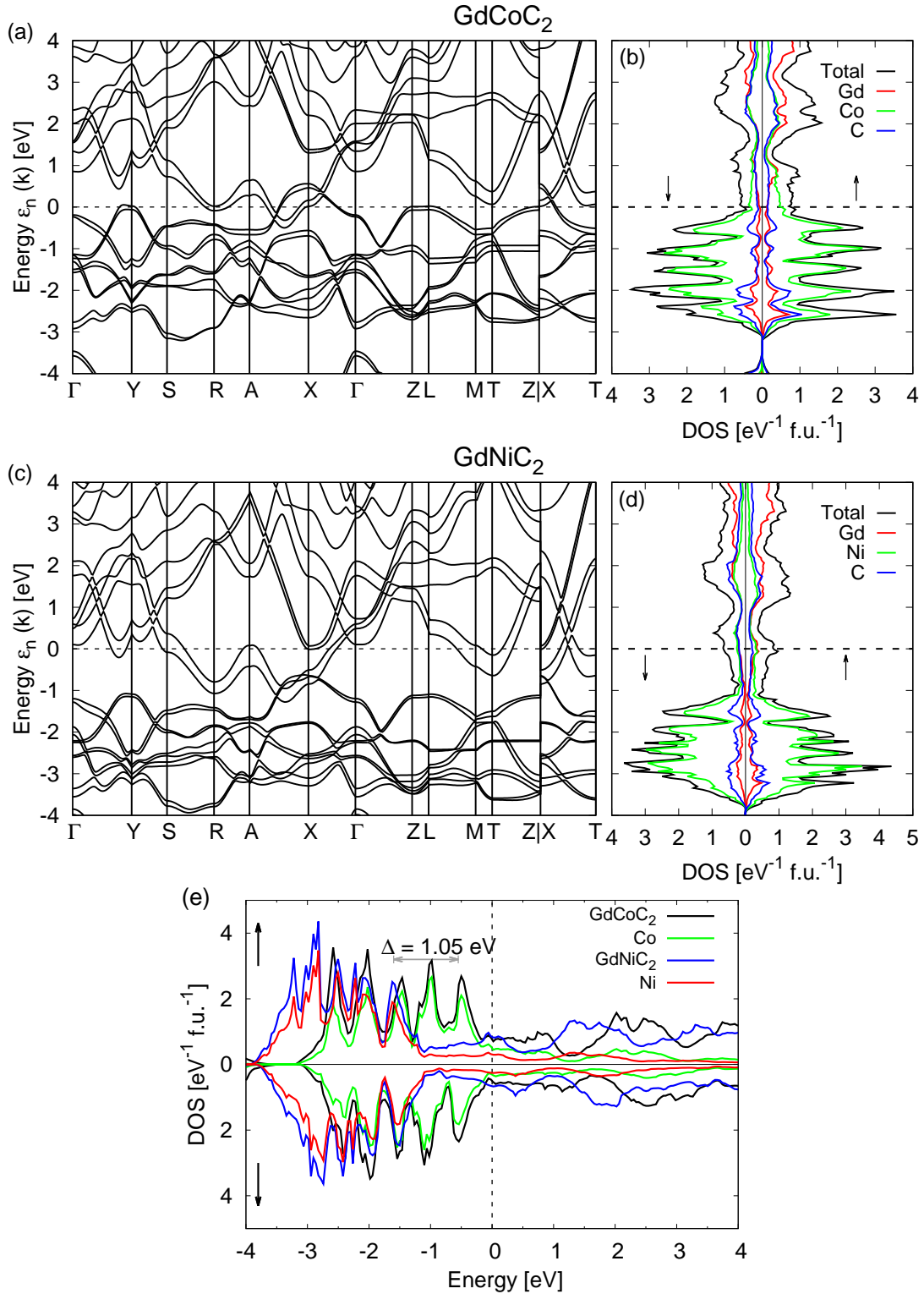


FIG. S5. Electronic properties of GdMC_2 : bandstructures, and DOS for (a)-(b) GdCoC_2 , (c)-(d) GdNiC_2 for the FM state with spin quantization axis $\mathbf{m} \parallel [001]$, as obtained within the OC approach and spin-orbit effects included. The BZ and the corresponding high-symmetry points are similar to that of YCoC_2 [see Fig. S3(c)]. The spin- and element-resolved partial DOS is also shown, where the spin components are indicated by arrows. A comparison of the total DOS and M-3d contribution to the DOS for both the compounds is shown in (e), clearly showing that the relative shift is only nominal ~ 1 eV.

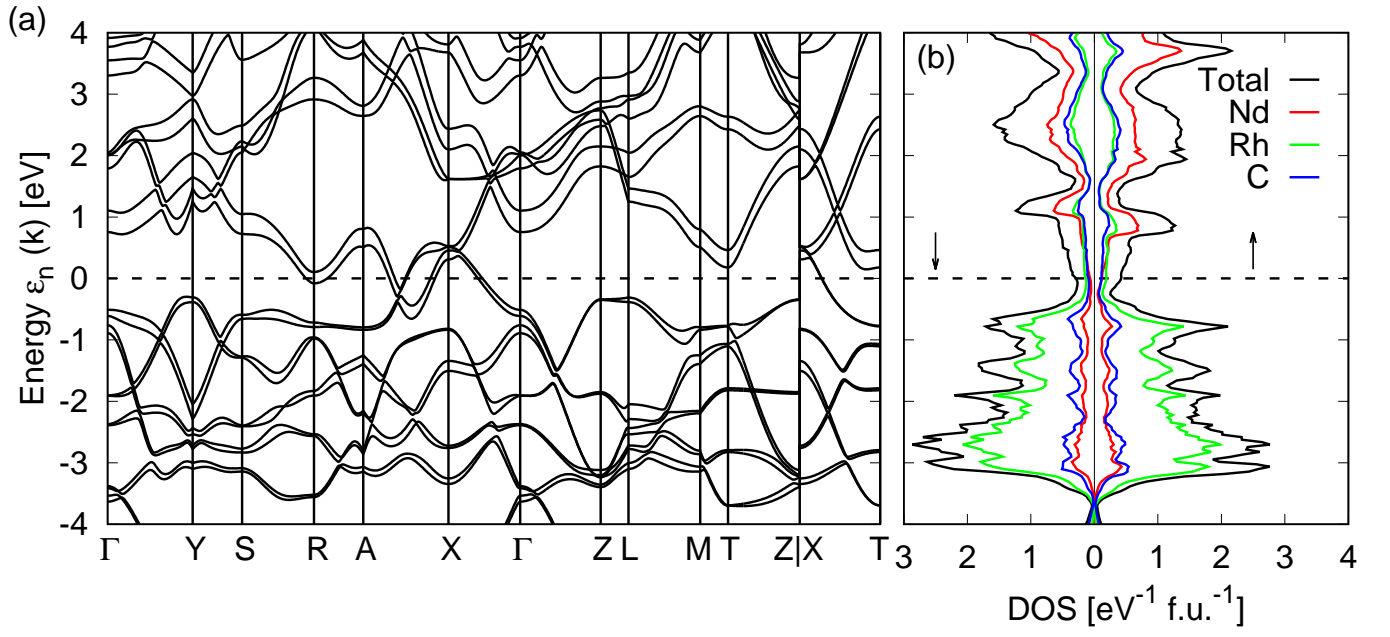


FIG. S6. Electronic properties of NdRhC_2 : bandstructure, and total and element-resolved DOS for the FM configuration with $\mathbf{m} \parallel [001]$, as obtained within the OC approach and spin-orbit effects included. For the position of the high-symmetry points in the Brillouin zone, see Fig. S3(c).

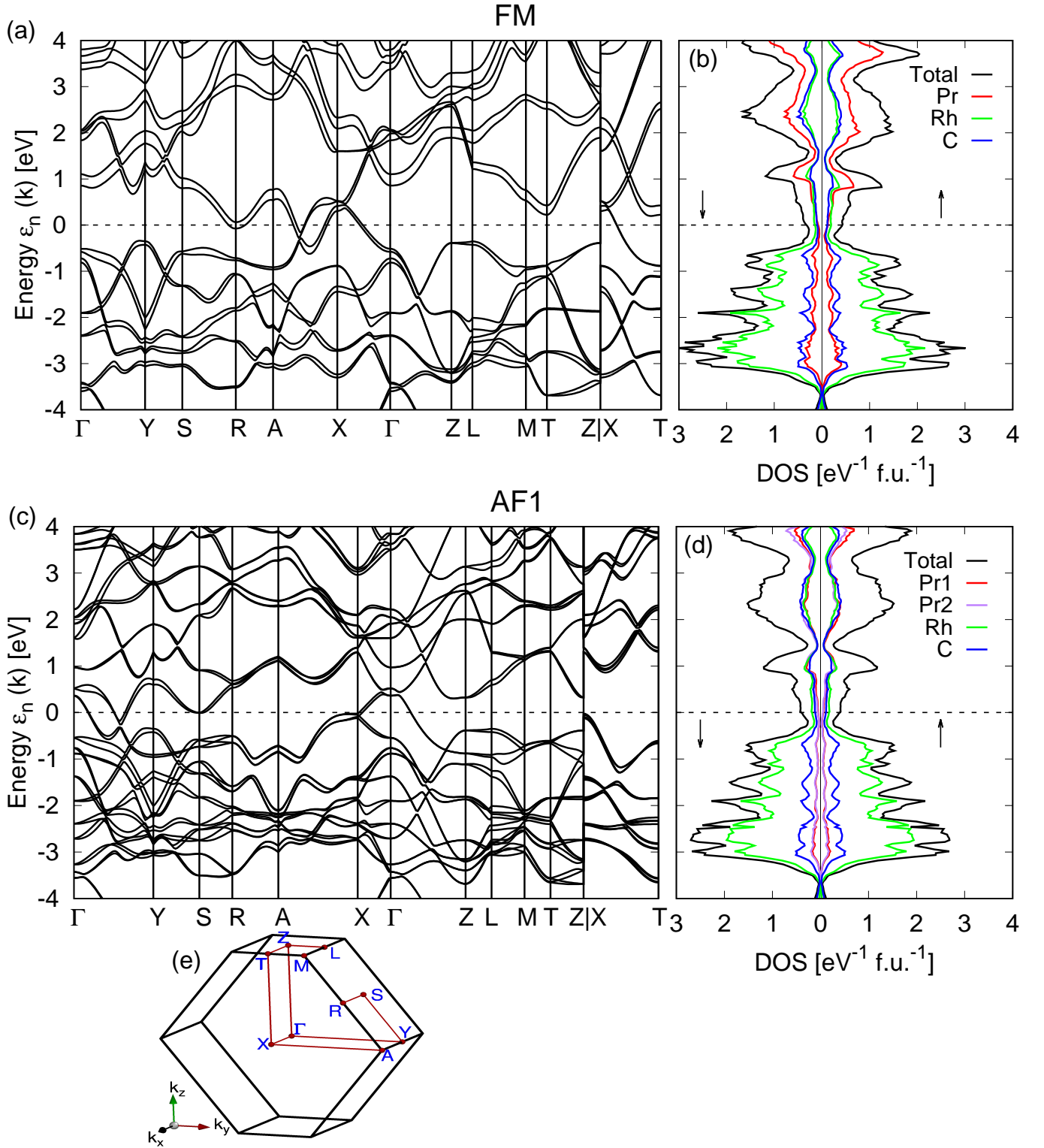


FIG. S7. Electronic properties of PrRhC_2 : bandstructure, and total and element-resolved DOS for (a)-(b) FM, and (c)-(d) AF1 magnetic configurations with $\mathbf{m} \parallel [001]$, as obtained within the OC approach and spin-orbit effects included. The BZ and the high-symmetry points for both the AF1 magnetic configuration is similar to FM, since the AF1 state corresponds to doubling of the unit cell along a (see Fig. S1), shown in (e).

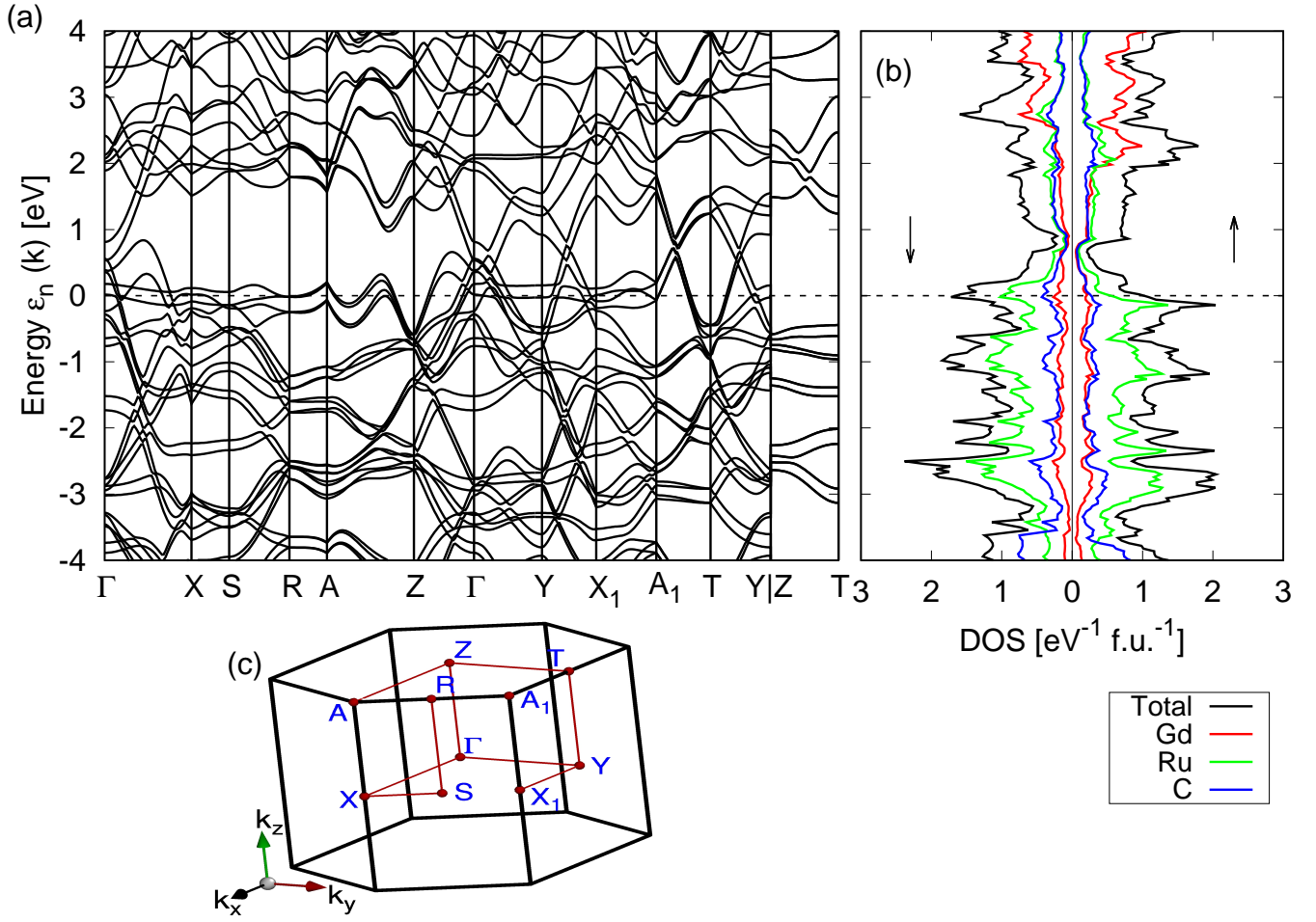


FIG. S8. Electronic properties of GdRuC_2 : (a) bandstructure, and (b) total and element-resolved DOS, as obtained within the OC approach and spin-orbit effects included. The high-symmetry points are shown in (c). Note that due to the different number of valence electrons as compared to GdCoC_2 , the band structure here is noticeably more complex at the Fermi energy and, therefore, GdRuC_2 should not be considered a semimetal.

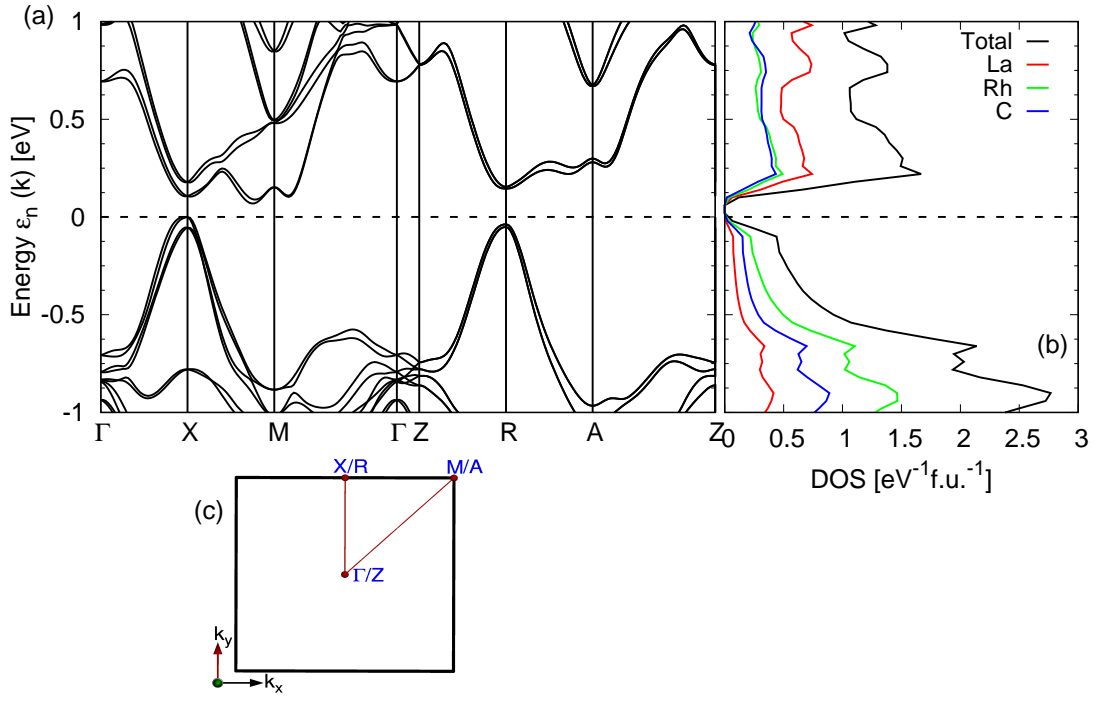


FIG. S9. (a) Bandstructure and (b) DOS for LaRhC_2 , as obtained using the GGA functional with spin-orbit effects included. The band gap is approximately ~ 84 meV. The high symmetry points in the Brillouin zone are depicted in (c).